White Rose Research Online

eprints@whiterose.ac.uk
https://eprints.whiterose.ac.uk
Universities of Leeds, Sheffield and York

Deposited via The University of Leeds.

White Rose Research Online URL for this paper:
https://eprints.whiterose.ac.uk/id/eprint/237276/

Version: Accepted Version

Article:
Wang, Y., Wignall, P.B., Mills, B.J.W. et al. (Accepted: 2026) Cooling-induced intensification of ocean anoxia in the mid-Paleozoic. Science Advances. ISSN: 2375-2548 (In Press)

This is an author produced version of an article accepted for publication in Science Advances, made available via the University of Leeds Research Outputs Policy under the terms of the Creative Commons Attribution License (CC-BY), which permits unrestricted use, distribution and reproduction in any medium, provided the original work is properly cited.

Reuse
This article is distributed under the terms of the Creative Commons Attribution (CC BY) licence. This licence allows you to distribute, remix, tweak, and build upon the work, even commercially, as long as you credit the authors for the original work. More information and the full terms of the licence here: https://creativecommons.org/licenses/

Takedown
If you consider content in White Rose Research Online to be in breach of UK law, please notify us by emailing eprints@whiterose.ac.uk including the URL of the record and the reason for the withdrawal request.

UNIVERSITY OF LEEDS
University of Sheffield
UNIVERSITY of York

Title: Cooling-induced intensification of ocean anoxia in the mid-Paleozoic

Authors: Yuxuan Wang[1,2*], Paul B. Wignall[1*], Benjamin J. W. Mills[1], Alexander J. Dickson[3], David K. Loydell[4], Yijun Xiong[1], Zhen Xu[1], Jeffrey Peakall[1], Simon W. Poulton[1*]

Affiliations

[1]School of Earth and Environment, University of Leeds, Leeds, LS2 9JT, UK

[2]Organic and Earth Surface Geochemistry, GFZ Helmholtz Centre for Geosciences, 14473, Potsdam, Germany

[3]Centre of Climate, Ocean and Atmosphere, Department of Earth Sciences, Royal Holloway University of London, Egham, TW20 0EX, UK

[4]School of the Environment and Life Sciences, University of Portsmouth, Burnaby Road, Portsmouth, PO1 3QL, UK

*Corresponding authors: YW (wyxleeds@gmail.com); PBW (p.b.wignall@leeds.ac.uk); SWP (s.poulton@leeds.ac.uk)

Abstract

Mid-Paleozoic oceanic anoxic events (OAEs) have long posed an enigma, with their drivers and dynamics being markedly distinct from the hyperthermal-related events of later eras. Here, we investigate a prominent mid-Silurian OAE, which was associated with the Ireviken Extinction Event (IEE) and coincided with a cooling climate. We apply Fe speciation, redox-sensitive trace metals and elemental weathering proxies, alongside sedimentological records and coupled uranium–molybdenum isotope analyses, to deep shelf and basinal sections from the UK. These data demonstrate a gradual spread of anoxia from basinal to shelfal settings, which we postulate was driven by an enhanced nutrient supply delivered via cooling-induced upwelling. Isotope mass balance modelling supports a major increase in the extent of deeper water ferruginous conditions at this time, while euxinia developed on the continental shelf, stressing the shallower water biota. A subsequent transition to ferruginous anoxia occurred on the shelf during the later stages of the event, as climatic conditions recovered and terrestrial chemical weathering rates increased. These changes, occurring when the ocean was poised at a lower redox state under the prevailing, low atmospheric oxygen levels of the mid-Paleozoic, led to oceanic anoxic event dynamics that were markedly different to those of the Mesozoic.

Introduction:

Silurian oceans underwent repeated perturbations that significantly impacted the global carbon cycle and the biosphere *(1-3)*. These episodes commonly led to enhanced ocean deoxygenation (termed oceanic anoxic events; OAEs) characterized by positive carbon

isotope excursions (CIEs), with prevalent examples being the early Sheinwoodian (ESCIE; ~432.5 Ma), mid-Homerian (~428.5 Ma) and mid-Ludfordian (~423.5 Ma) events *(4-8)*. However, unlike Mesozoic OAEs, which are generally associated with hyperthermals, Paleozoic examples have been linked to intervals of cooling *(1,5,9)*. Paleozoic OAEs are also distinct from their Mesozoic counterparts in that they occurred against a backdrop of generally low atmospheric and oceanic oxygenation levels, whilst near-modern levels of oxygenation only developed during the late Silurian to Devonian (the Paleozoic Oxygenation Event) *(10,11)*.

Many models for Paleozoic OAEs nevertheless invoke similar conditions to those proposed for Mesozoic OAEs *(12,13)*, while others emphasize distinctive Paleozoic features, including the absence of a link to major flood basalt eruptions *(14)*, and the general prevalence of a background oceanic state characterized by expanded ferruginous anoxia *(15)*. Overall, the causes of Paleozoic OAEs remain poorly understood. Here, we focus on the OAE that spans the latest Telychian to Sheinwoodian stages of the Silurian, which occurred in association with global cooling *(5,16)*. The interval includes the ESCIE *(17,18)* and is associated with the Ireviken Extinction Event (IEE), which saw severe losses amongst conodonts and graptolites *(19,20)*, and a major turnover of acritarchs *(21)*.

We investigate Llandovery–Wenlock boundary sections from the River Banwy in Wales and Ashgill Beck in England. These record outer shelf to basin settings on the Eastern Avalonian margin between Laurentia and Baltica (see Supplementary Materials) *(22,23)*. We reconstruct oceanic redox dynamics and climate using Fe speciation, redox-sensitive trace metals and elemental weathering proxies. Global redox variability is assessed using U and

Mo isotope data within the framework of a coupled U-Mo isotope mass balance model. Our approach allows a generic model to be developed for the enhancement of ocean anoxia during cooling intervals in the distinctive oceans of the mid-Paleozoic.

Progressive oxygen loss from basin to shelf

Initial insight into the evolution of water column redox conditions is provided by sedimentological constraints. The Banwy River section begins with predominantly light grey mudrocks through much of the Telychian (*crispus* to *lapworthi* biozones), interspersed with a distinct red bed interval (Fig. 2). Dark grey, laminated mudrocks appear in the *insectus* Biozone and initially alternate with paler, moderately burrowed mudrocks, until a persistent succession of dark, laminated mudrocks develops in the *riccartonensis* Biozone (lower Sheinwoodian). This indicates an overall progression to more poorly oxygenated conditions. At Ashgill Beck, where most of the Telychian is not exposed, a transition from pale grey, burrowed mudstones to dark grey laminated shales occurs abruptly in the upper Telychian, around the base of, or within, the *centrifugus* Biozone (Fig. 2).

To provide a more nuanced reconstruction of regional water column redox conditions, we utilize Fe speciation and redox-sensitive trace metal (RSTM) systematics (see Methods for analytical techniques, and Supplementary Materials for details of the redox proxy framework, as well as all data). Oxic baseline values for Fe speciation and RSTMs have previously been defined for the Welsh Basin (WBO) *(3)*, allowing a particularly refined reconstruction of the evolution of ocean redox conditions (see Supplementary Materials). With the exception of the red bed interval, highly reactive iron to total iron (Fe_{HR}/Fe_T) ratios are low throughout most of the Telychian (*crispus* to *insectus* biozones) in the Banwy River section (Fig. 2), suggesting that the deep outer shelf was not anoxic *(26)*. This inference is supported by low concentrations (around the WBO value) of redox-sensitive trace elements (U, Mo) (Figs. S2 and S3). However, Re/Mo ratios (Fig. 2) are commonly elevated through

this interval (again with the exception of the red beds), suggesting that bottom waters may have been at least intermittently dysoxic, rather than fully oxic *(27)* (see Supplementary Materials).

The red marine mudstones at Banwy River are the local manifestation of a global red bed interval found in deep water to outer-shelf settings during the middle Telychian *(28-30)*. The red mudstones have higher Fe_{HR}/Fe_T ratios compared to the interbedded mudrocks, due to enrichment in Fe oxides (particularly hematite (Fe_{ox}); Fig. 2). Persistently low U/Al and Mo/Al ratios (Fig. S2), coupled with a drop in Re/Mo ratios to WBO values (Fig. 2), imply well-oxygenated bottom water conditions during red bed formation *(27)*.

Above this transitional zone, the occurrence of highly elevated Fe_{HR}/Fe_T and Fe_{py}/Fe_{HR} ratios, which persist up until the peak of the ESCIE, suggests the initial development of euxinic water column conditions on the deep shelf (Fig. 2). This inference is supported by increased Mo/U and low Re/Mo ratios, alongside heavy $\delta^{34}S_{py}$ values (Fig. 2). However, Mo/U ratios are only moderately elevated, likely indicating relatively low concentrations of sulfide in the water column *(27)* (i.e., weakly euxinic conditions). While Fe_{HR}/Fe_T ratios remain elevated during the falling stage of the ESCIE, there is a distinct decline in Fe_{py}/Fe_{HR} ratios, to values that suggest a recovery to ferruginous anoxia. This is supported by a subtle decline in $\delta^{34}S_{py}$ values and Mo/U ratios, as well as an increase in Re/Mo ratios, all of which are consistent with lower levels of sulfide production *(27)*.

In the deeper water Ashgill Beck setting, Re/Mo values vary at the bottom of the section (Fig. 2), with some highly elevated values indicating the development of dysoxic conditions in grey mudstones, while samples with lower Re/Mo and elevated U/Al (Fig. S2) suggest

fluctuations to fully anoxic conditions. However, anoxic grey mudstone samples, as well as anoxic black shales at the base of the overlying strata, have low Fe_{HR}/Fe_T ratios, suggesting that the sediments were a source of Fe^{2+} to the water column (giving low Fe_{HR}/Fe_T ratios *(31)*).

The transition to persistently anoxic conditions in the *centrifugus* Biozone at Ashgill Beck precedes the development of persistent anoxia observed in the shallower water Banwy River section, where the transition occurs in the later *riccartonensis* Biozone (a delay of ~1.5 Myr according to a recent age model *(32)*) (Fig. 2). Persistently elevated Fe_{HR}/Fe_T ratios, low Re/Mo ratios and high $d^{34}S_{py}$ values, combined with variable Fe_{py}/Fe_{HR} and Mo/U ratios, suggest alternations between ferruginous and euxinic anoxia *(27,31)* in deeper waters throughout the ESCIE interval (Fig. 2).

The redox dynamics evident in deeper and shallower waters suggest that, prior to the development of more persistent, expanded anoxia, the water column was dominantly characterized by dysoxic-anoxicconditions. In deeper waters, this background redox state would have allowed Fe^{2+} to build-up in the water column *(31)*. The elevated Fe_{HR}/Fe_T ratios that occur during the red bed interval thus likely reflect water column precipitation of dissolved Fe^{2+}, whereby a transient episode of more expansive global oxygenation (see below) resulted in a deepening of the oxycline, which impinged on the deeper ferruginous waters *(31)*. The alternative, that an enhanced continental weathering influx of Fe oxides drove the global deposition of red beds at this time *(29,33)*, is not supported by the chemical index of alteration (CIA) record in the River Banwy section, which does not change across the red bed interval (Fig. 2). Specifically, a globally-enhanced supply of Fe oxides to the

marine realm requires a major increase in chemical weathering intensity on land *(34, 35)*, which should be reflected by higher CIA values. Furthermore, while local depositional factors such as hydraulic sorting and sediment provenance may influence Fe enrichment, such factors would not be expected to occur contemporaneously on a global scale. Later in the Telychian, the oxycline shallowed again, resulting in the re-expansion of dysoxic-ferruginous conditions, before the development of more intense and persistent deeper water anoxia coincident with the onset of the ESCIE, with anoxic conditions then expanding into shallower water settings.

Constraining global redox conditions

Due to their prolonged residence time (>400 kyr) and distinct redox-driven fractionation effects, U and Mo stable isotopes ($\delta^{238}U$ and $\delta^{98}Mo$) can aid reconstruction of past global oceanic redox conditions *(36-38)*. We first note that there is no correlation between either U and Al, or U and TOC (Figs. S7 and S8), suggesting negligible detrital or productivity influence on $\delta^{238}U$ compositions *(39)*, and thus redox variability was likely the dominant control. There is also no systematic difference between the $\delta^{238}U$ composition of ferruginous (-0.29 ± 0.05) and weakly euxinic (-0.28 ± 0.05) samples, consistent with the persistence of redox conditions amenable to U(VI)–U(IV) reduction across the sediment-water interface (similar to the Fe(III)–(II) redox couple) *(40)*.

Only four oxic samples (from the Banwy River section) contained sufficient Mo for isotopic analysis (Fig. 2), including three oxic samples from the red beds, which have negative $\delta^{98}Mo$ values (-1.50 ± 0.05‰), and an underlying grey mudstone sample that has a particularly low value (-2.39‰). These red bed data suggest uptake of Mo to Fe

(oxyhydr)oxides precipitating under oxic conditions *(41)*, while the very low value in the grey mudstone could reflect repeated cycles of Fe (and potentially Mn) reduction and re-oxidation in pore waters *(41,42)* under the fluctuating redox conditions proposed for this interval in the Banwy River section, or non-quantitative Mo-sulfide burial under weakly sulfidic conditions within the sediments. For anoxic samples, δ^{98}Mo data show no systematic covariation with either TOC or Al contents (Figs. S7, S8), again indicating that local changes in productivity or detrital influx exerted minimal influence on δ^{98}Mo variability. However, the δ^{98}Mo values for these samples show considerable variability (Fig. 2), suggesting partial drawdown of Mo under both weakly euxinic and/or ferruginous conditions (where Mo may have been sequestered in sulfidic porewaters or via uptake to Fe (oxyhydr)oxides), rather than complete drawdown of Mo, which requires high water column sulfide concentrations coupled with limited seawater renewal *(43,44)*.

Simulating mid-Paleozoic OAE dynamics

To provide a quantitative assessment of the seafloor redox landscape during the ESCIE, we applied a modified isotope mass balance model *(45-47)* that integrates U and Mo isotope data (Figs. 3, S10). The model accounts for U and Mo burial under oxic, ferruginous and euxinic conditions, and in the model runs we randomly vary the fractions of the seafloor that experience each of these redox regimes, in order to predict the isotopic compositions of U and Mo buried in these areas. We then compare this large suite of model predictions to our isotope data for Mo and U buried in oxic or ferruginous conditions, to infer the most likely redox composition of the seafloor throughout the studied time interval. Figure 3 presents these results as a ‘cost function’, which represents the overall difference between

the isotope measurements and the model predictions. Here, the lowest cost function value indicates the most likely seafloor redox landscape, and is highlighted by a dashed perimeter line (Fig. 3C, D; see Supplementary Materials for further model details).

Due to the lack of Mo isotope data for the non-red bed pre-OAE interval, our focus was on modelling the red bed interval, which appears to represent the maximum extent of pre-OAE oxygenation, as well as the OAE itself (Fig. 3). During the red bed interval, we find that the most plausible scenario to account for the observed U and Mo isotopic compositions involves approximately 5% of the global seafloor being ferruginous, with less than 1% being euxinic. By contrast, during the onset and aftermath of the ESCIE, the ferruginous seafloor area increased towards 100%, while euxinic areas remained low, but may have increased modestly (Fig. 3). This overall degree of deoxygenation substantially exceeds that observed during most Mesozoic OAEs, where anoxia typically bathed less than 10% of the ocean floor *(15,48)* (Fig. S12).

While we do not specifically utilize our coupled U-Mo isotope model to quantify the background (i.e., non-red bed) extent of anoxia prior to the OAE itself, we note that samples deposited in the transitional and anoxic zones (Fig. 2) have similar $\delta^{238}U$ ranges (-0.28 ± 0.05) relative to the underlying Telychian strata (-0.33 ± 0.04). On a qualitative level, this implies a relatively minor change in the global extent of anoxia *(49,50)*, as anoxic conditions expanded from the deep ocean into shallower environments, which may be expected given that the deep marine realm (>1000 m) comprises over 99% of the ocean's volume and 89% of its seafloor surface *(51)*. However, while deoxygenation driven by upwelling ferruginous deep waters may not have significantly expanded the anoxic U sink, the implications of an

expansion of anoxia into shallow waters, coupled with the specific development of shallower water euxinia, are particularly profound (see below).

A cooling-driven mechanism for Paleozoic ocean anoxia

Our interpretation of expansive dysoxic-anoxic conditions in the deep ocean during non-red bed intervals of the mid Telychian is supported by independent evidence for hypoxic Silurian oceans *(52)*. However, the underlying reason for the temporally-limited expansion of well-oxygenated conditions during the red bed interval is unclear and requires further study. Nevertheless, our data do provide insight into the factors that controlled the subsequent expansion of anoxia into shallower water environments during the OAE itself.

Multiple independent lines of evidence (see Supplementary Materials) support a progressive drop in chemical weathering linked to global cooling, beginning with the late Telychian glaciation *(25)* prior to the onset of expanded ocean anoxia, which was then followed by the mid-Sheinwoodian glaciation *(5)* (Fig. 4). Consistent with this change, CIA values in the Banwy River section show a decline in chemical weathering intensity beginning in the late Telychian *spiralis* Biozone and reaching a nadir in the Sheinwoodian *firmus* Biozone (Fig. 2). This is followed by a return to higher values as chemical weathering increased during the later part of the ESCIE (Fig. 2). In contrast to Mesozoic OAEs *(55)*, this suggests that the development of expansive anoxia was linked to a decrease in the chemical weathering influx of key nutrients such as phosphorus, rather than an increase.

We thus propose a new OAE mechanism for the mid-Paleozoic in which cooling amplified the temperature contrast between equatorial and high-latitude seawater, intensifying ocean circulation (Fig. 3). Consequent increased downwelling at high latitudes

increased upwelling of ferruginous seawater at lower latitudes, delivering anoxic waters to outer shelf regions (e.g., the Banwy River section). The upwelling of nutrient-rich deep waters would have stimulated productivity along continental margins, with globally-enhanced organic carbon burial occurring as extensive, deoxygenated shelf seas developed (as indicated by peak $\delta^{13}C_{org}$ values occurring coincident with the development of persistent anoxia on the shelf; Fig. 2). Temperature and sea-level records for the Telychian–Sheinwoodian interval show that the gradual onset of the ESCIE coincides with cooling and glacioeustatic sea-level fall *(20,54)*. Our model scenario thus suggests that under the relatively low atmospheric oxygen levels of the mid-Paleozoic, a modest increase in the flux of nutrients to the photic zone from upwelling was able to drive expansive shallow water deoxygenation.

These climate-driven weathering dynamics also help to explain the chemistry of anoxic waters during the ESCIE. Relatively enhanced chemical weathering promotes more extensive generation of reactive Fe mineral phases from parent silicate minerals, which ultimately promotes ferruginous anoxia, rather than euxinia *(25)*. This is consistent with the development of more widespread euxinia at the peak of the OAE, but as the climatic state recovered (as indicated by an increase in CIA values towards the top of the Banwy River section), more intense weathering promoted more expansive ferruginous anoxia (Fig. 2). This, in turn, would have resulted in more efficient trapping of phosphorus in association with Fe minerals, thereby resulting in a negative productivity feedback that would have limited organic carbon production and burial *(56,57)*, hence aiding recovery from the expansive OAE and the ESCIE.

Despite the relatively poorly ventilated oceans of the mid-Paleozoic, marine invertebrates thrived and underwent major radiations during both the Ordovician and the recovery interval following the Late Ordovician mass extinction (LOME) *(58)*. By implication, many taxa must have been tolerant of, and able to radiate in, poorly oxygenated oceans *(52)*. Despite this innate tolerance, the expansion of anoxic waters into shelf habitats led to the extinction losses of the IEE, and this appears to have been particularly exacerbated by the development of euxinia in shelf settings *(3)*. In some regards the IEE is thus comparable to younger marine extinction crises in which OAEs, and in particular the development of euxinia, are implicated *(59)*, but the associated link with transgression and global warming is absent in the Silurian. Instead, global cooling appears to have been the ultimate driver of the major biotic crisis that occurred during the IEE, and by extension, other mid-Paleozoic intervals of anoxia when similar environmental perturbations occurred.

Figure captions

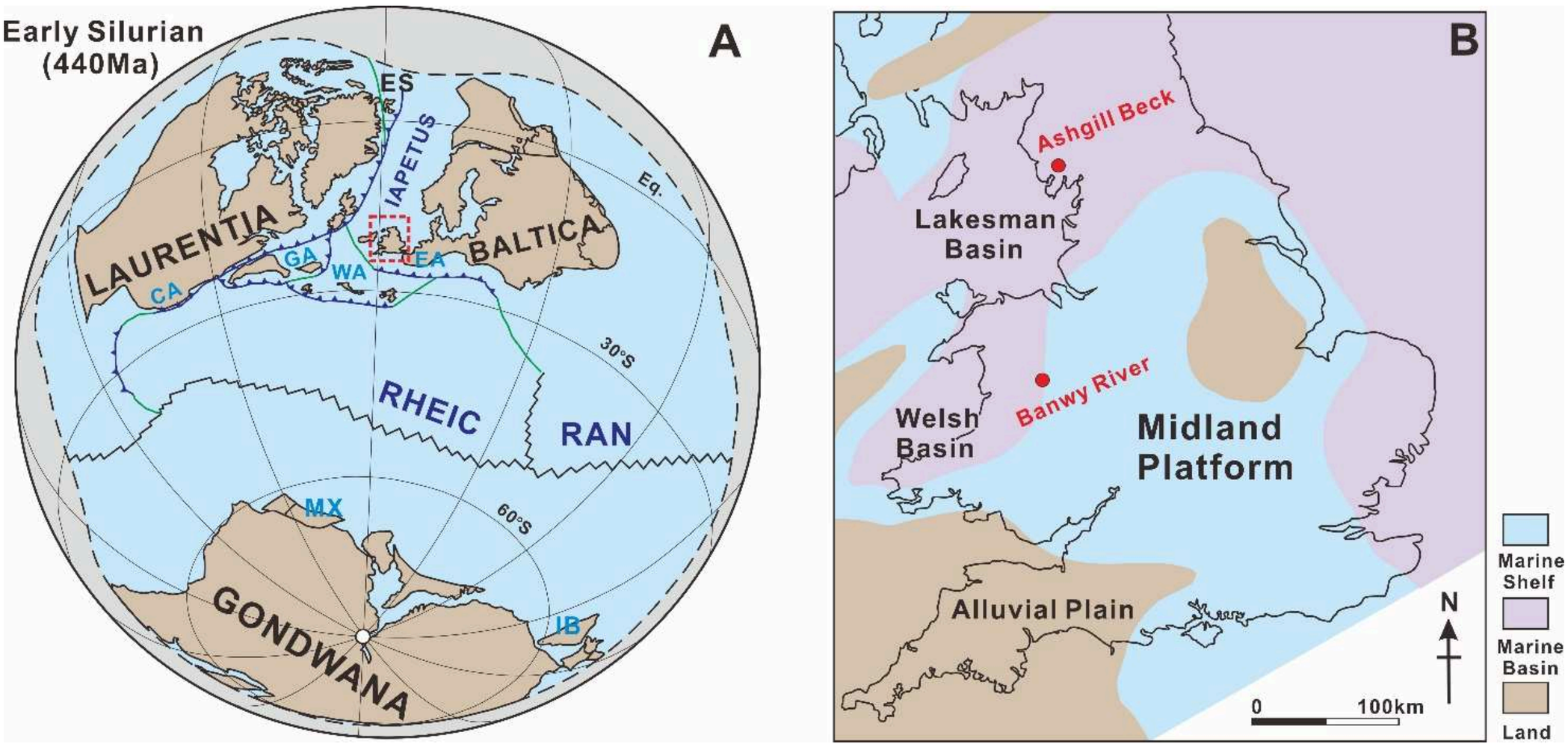

Fig. 1. Paleogeographic context of the Silurian study area. A. Global reconstruction of paleogeography during the Llandovery (adapted from *(24)*; CA: Carolinia, GA: Ganderia, WA: West Avalonia, EA: East Avalonia, MX: Mixteca-Oaxaca, IB: Iberia. Solid blue lines represent subduction zones, black lines represent spreading centers, and green lines represent transform plate margins. B. Paleogeography of the UK during the mid-Silurian. (modified after British Geological Survey web graph, https://earthwise.bgs.ac.uk).

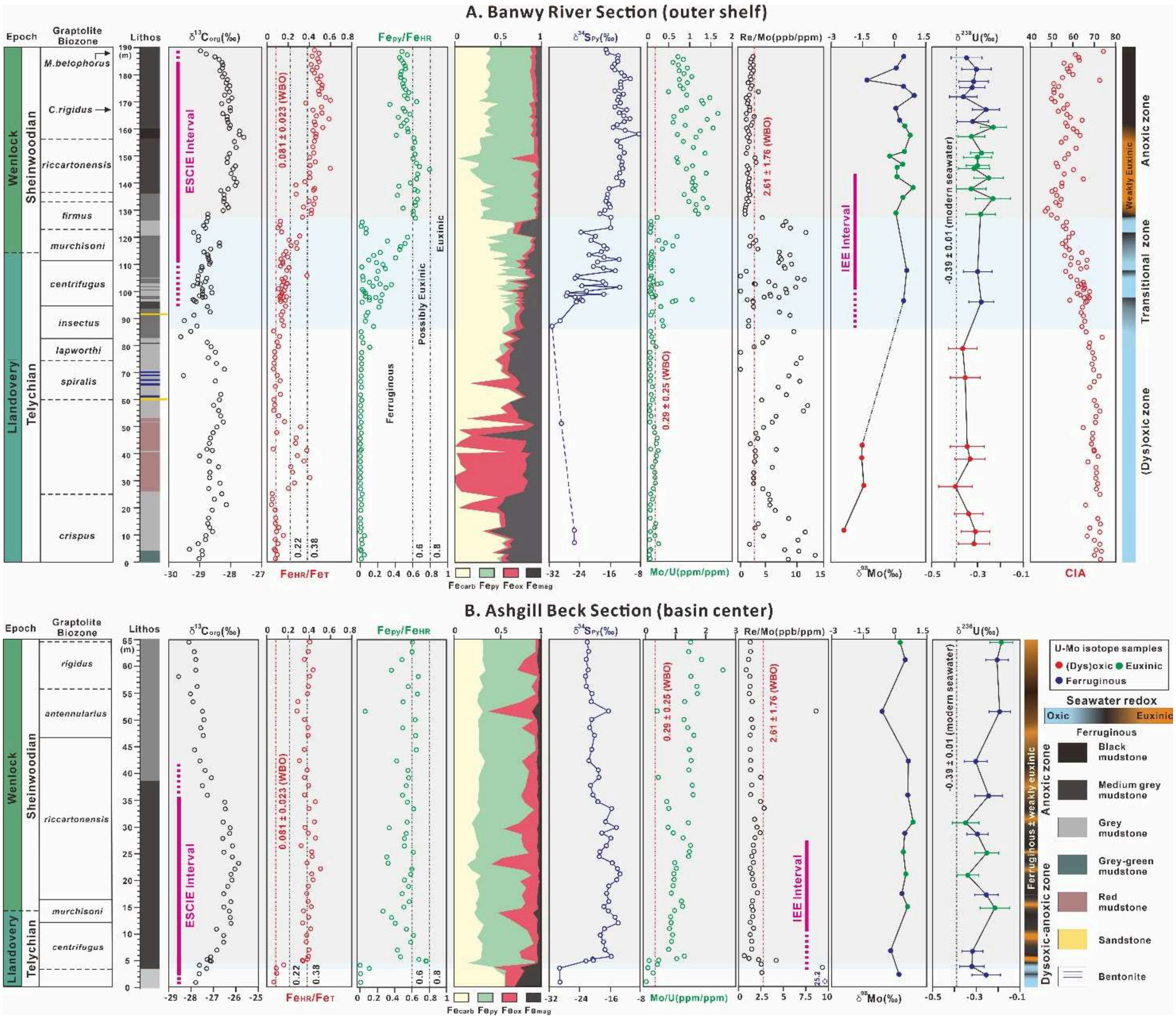

Fig. 2. Stratigraphy and redox proxies from shelf to basin. Stratigraphic and geochemical data for the deep-shelf Banwy River section (A) and the basinal Ashgill Beck section (B). Graptolite biozones are from published studies *(23,25)*. Dashed line on the Fe_{HR}/Fe_T plot represents the Welsh Basin oxic (WBO) baseline, while dashed lines on the redox-sensitive trace metal plots represent the WBO composition *(3)*. On the Fe_{HR}/Fe_T plot, published thresholds for general identification of oxic (<0.22), possibly anoxic (0.22-0.38) and anoxic (>0.38) water column conditions *(26)* are included for context. However, in this case, these thresholds are superseded by our regional oxic baseline calibration (WBO). Dashed lines on the Fe_{py}/Fe_{HR} plot represent calibrated thresholds for the identification of ferruginous (<0.6),

possibly euxinic (0.6-0.8), and euxinic (>0.8) depositional conditions for anoxic samples *(26,31)*. Pale blue shading indicates the transitional redox zone, while pale grey shading indicates water column anoxia. Uncertainties for Mo-isotope data are smaller than the symbol size.

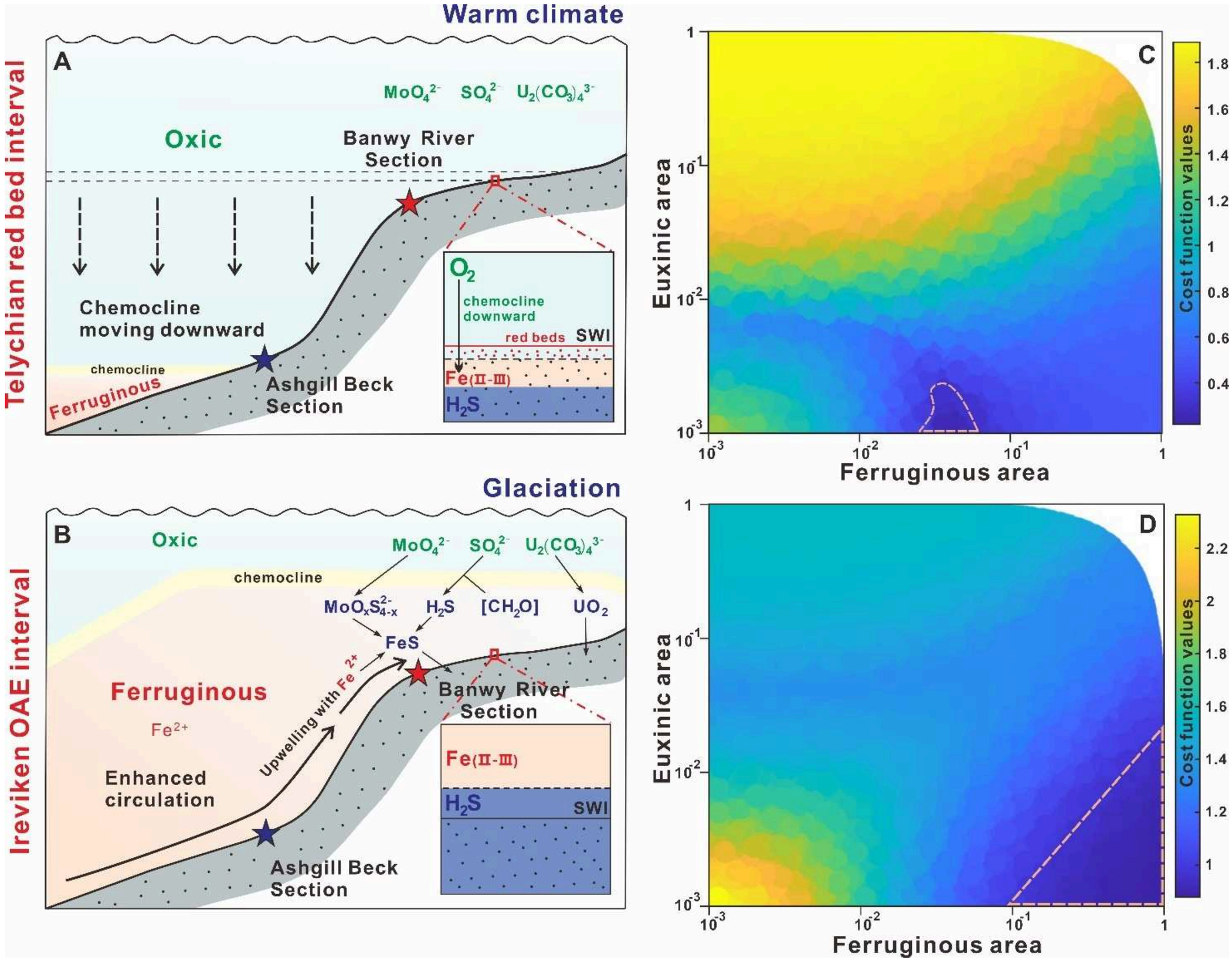

Fig. 3. Modeling redox evolution during Silurian anoxia. Schematic showing the evolution of the basinal redox structure and key chemical and physical processes during the Telychian red bed interval (A) and the Ireviken OAE interval (B). U-Mo isotope mass balance model outputs for the Telychian oxygenation interval (C) and the Ireviken OAE interval (D). Colours represent the mathematical distance between 100,000 model runs and measured U and Mo

isotope values. The areas enclosed by dashed lines represent the most likely redox scenarios.

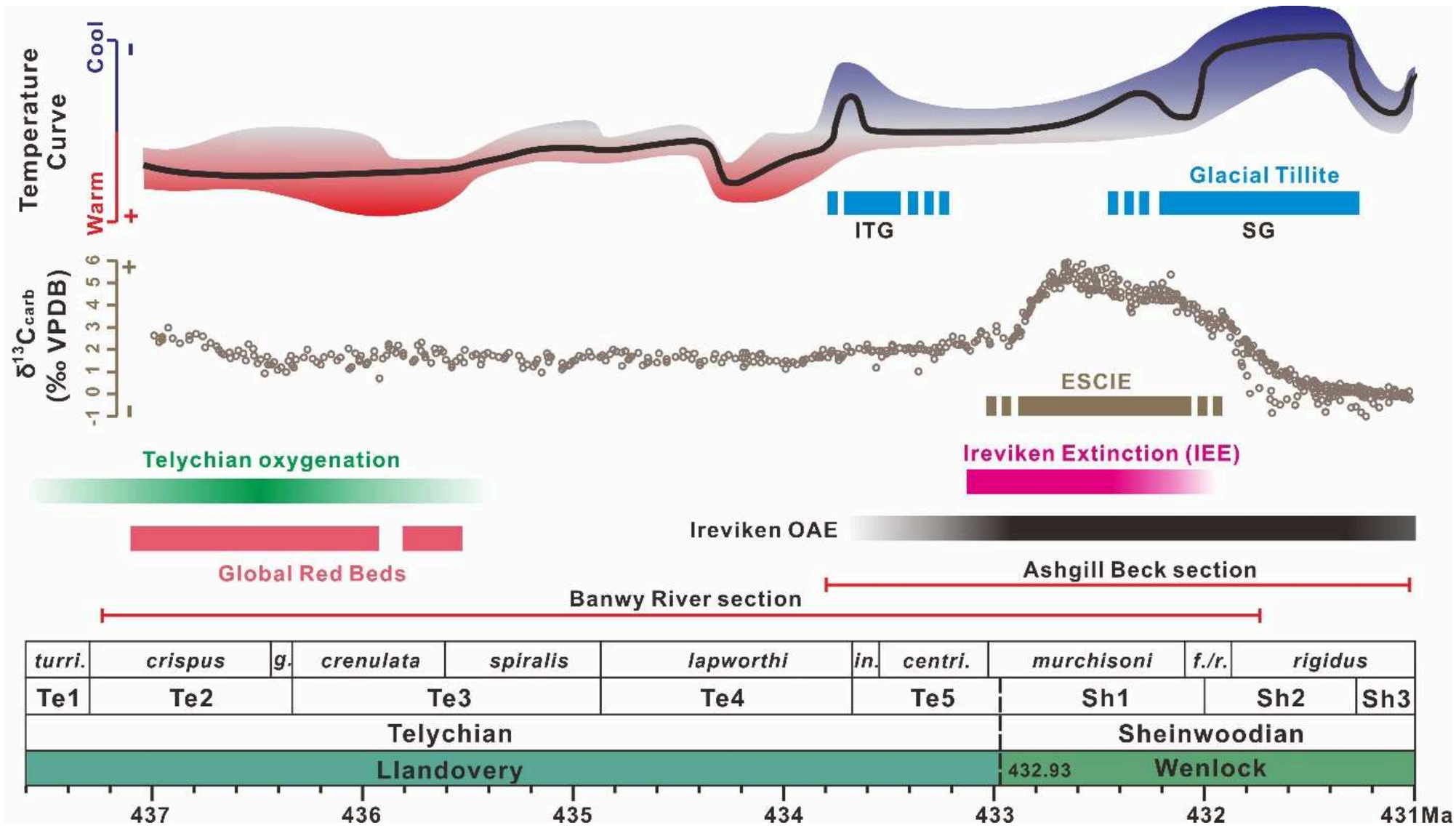

Fig. 4. Environmental and redox changes across the Llandovery–Wenlock boundary. Summary of key environmental events and the evolution of ocean redox conditions across the Llandovery–Wenlock boundary in the early Silurian. The $\delta^{13}C_{carb}$ data are adapted from *(53)*; the late Telychian glaciation (lTG) is from *(54)*; the mid-Sheinwoodian glaciation (SG) is from *(5)*; the $\delta^{18}O$-derived temperature records for Baltica are based on *(16)*. All records are calibrated to the Geologic Time Scale 2020 *(53)*. See Supplementary Materials for further details of these key environmental records. Abbreviations: *turri. = turriculatus; g. = griestoniensis; in.= insectus; centri. = centrifugus; f. = firmus; r. = riccartonensis*.

Materials and Methods

Organic carbon concentrations and isotopes

For total organic carbon and organic carbon isotope ($\delta^{13}C_{org}$) analyses, samples were pre-treated with 10% HCl to remove carbonate, prior to analysis in the Cohen Laboratories, University of Leeds. Total organic carbon was determined on a LECO CS-230 analyser, with replicate analyses of a certified standard (Soil 502–309, n=24) giving a relative standard deviation (RSD) of <3%, with measurements within 2% of certified values.

The $\delta^{13}C_{org}$ compositions were determined on an Elementar PYRO cube coupled to an IsoPrime continuous flow mass spectrometer. Results are given in δ notation calibrated to the Vienna-Pee Dee Belemnite (V-PDB) scale, using UREA and sucrose laboratory standards of known isotopic composition (UREA by Merck with $\delta^{13}C$ = -46.83 ± 0.22‰; Silver Spoon sucrose (commercial) with $\delta^{13}C$ = -26.19 ± 0.10‰; T&L sucrose (commercial) with $\delta^{13}C$ = -11.93 ± 0.24‰). Standard reproducibility given by repeat analyses of the internal sucrose standard was better than 0.1‰ (1 SD).

Iron speciation and pyrite S isotopes

Unsulfidized iron phases were quantified using a sequential extraction scheme *(60)* in the Cohen Laboratories, University of Leeds. This operationally-defined procedure targets Fe present in carbonate phases (Fe_{carb}), as Fe (oxyhydr)oxides (Fe_{ox}), and in magnetite (Fe_{mag}). The Fe_{carb} phase was extracted using Na-acetate solution at pH 4.5 and 50°C for 48 h. The residue was then treated with Na-dithionate for 2 h at room temperature to extract Fe_{ox}. Finally, Fe_{mag} was extracted with ammonium oxalate solution for 6 h at room temperature. All extractant solutions were then measured for Fe by atomic absorption spectrometry.

Sulphide-bound Fe, including acid volatile sulphide Fe (Fe_{AVS}, below detection in all cases) and pyrite (Fe_{py}) were extracted by the two-step hydrochloric acid (HCl) and chromous chloride ($CrCl_2$) method *(61)*. The released H_2S was precipitated as Ag_2S, which was then determined gravimetrically. Replicate analyses (n=8) of the international reference material, WHIT *(62)*, gave RSDs of <5% of all Fe phases.

Sulphur isotope ($\delta^{34}S_{py}$) analyses were performed on the Ag_2S precipitates using an Elementar PYRO cube coupled to an IsoPrime continuous flow mass spectrometer in the Cohen Laboratories, University of Leeds. Calibration to the Vienna-Canyon Diablo Troilite (V-CDT) scale was performed using a barium sulphate standard, SWS-3A (assigned $\delta^{34}S$ = 20.3‰), and an inter-lab standard, CP-1 (chalcopyrite; assigned $\delta^{34}S$ = -4.56‰), validated against internationally recognized reference materials NBS-127 (20.3‰), NBS-123 (17.01‰), IAEA S-1 (−0.30‰) and IAEA S-3 (−32.06‰). Precision was verified through repeat measurements of the CP-1 standard, yielding a value of ±0.15‰ (1 SD).

Major and trace elements

Samples were initially ashed at 550℃ for 8 h, followed by dissolution with a mixture of HNO_3, HF and $HClO_4$. After evaporation to dryness, samples were treated with boric acid (H_3BO_3) to ensure full solubilization of Al hexafluorates, and heated to dryness before being re-dissolved in hot HNO_3. Total element concentrations were subsequently determined using ICP-OES (ThermoFisher iCAP 7400) for major elements (Al, Fe, Mn) and ICP-MS (ThermoFisher iCAPQc) for trace elements (U, Mo, Re). Replicate extractions of international sediment standard SGR-1 yielded RSDs of<5% for all elements of interest, and analyses were within 3% of certified values.

Uranium and molybdenum isotopes

Uranium and Mo isotope analyses were performed in an ISO6 metal-free clean laboratory at Royal Holloway, University of London. Samples were precisely weighed (to give more than ~300 ng Mo and ~100 ng U) and combined with an aliquot of either a ^{97}Mo-^{100}Mo double spike or an IRMM 3636a ^{236}U-^{233}U double spike, to give a Mo spike/sample ratio of ~ 0.3 and a U spike/sample ratio of ~0.1. Samples were then digested with a concentrated mixture of HNO_3 and HCl (in a 3:1 ratio) at 150℃ to dissolve the non-detrital fraction. Mo and U were purified from the sample matrix following chromatography protocols using AG1-X8 200–400 dry mesh resin *(63, 64)* and Eichrom UTEVA resin *(65)*. Both isotopes were measured on a Thermo-Finnigan Neptune Plus multi-collector inductively coupled plasma mass spectrometer equipped with a CETAC Aridus III desolvating nebulizer system for sample introduction. An acid blank was measured before each sample to correct for memory effects during sample washout. Isotope compositions were calculated relative to NIST 3134 for Mo, and CRM112a standard for U:

$$\delta^{98}Mo\ (‰) = [(^{98}Mo_{sample}/^{95}Mo_{sample}) / (^{98}Mo/^{95}Mo_{NIST3134}) - 1] \times 1000 + 0.25 \quad (1)$$

$$\delta^{238}U\ (‰) = [(^{238}U_{sample}/^{235}U_{sample})/(^{238}U/^{235}_{CRM112a}) - 1] \times 1000 \quad (2)$$

Replicate measurements of the Open University (OU) standard relative to NIST 3134 yielded a mean value of -0.36 ± 0.05‰ (2 SD; n=6), with results being within uncertainty of the reported value of -0.37‰ *(66)*. Replicate measurements of certified SDO-1 and SGR-1 standards yielded values of 1.03 ± 0.05‰ (2 SD, n=4) and 0.66 ± 0.10‰ (2 SD, n=4), respectively, which are similar to published values of 1.05 ± 0.14‰ *(66)* and 0.68 ± 0.05‰ *(67)*. For $\delta^{238}U$, repeat measurements of the SDO-1 and SGR-1 standards yielded values of

-0.08 ± 0.08‰ (2 SD, n=4) and -0.22 ± 0.09‰ (2 SD, n=4), respectively, which are similar to previous study values of -0.07 ± 0.03‰ *(68)* and -0.17 ± 0.02‰ *(68)*. Total procedural blanks measured by isotope dilution were negligible for both isotopes.

Joint U-Mo mass balance model

We utilized an updated dynamic mass balance model *(46)* for U and Mo cycling in the global ocean (see parameters in Table S6), where the integrated input and output fluxes control the seawater inventory and isotopic composition of both elements:

$$\frac{d[M]_{sw}}{dt} = F_{input} - F_{output} \quad (3)$$

$$\frac{d[M]_{sw}}{dt} \cdot$$

$$\delta M_{sw} = F_{input} \cdot \delta_{input} - F_{output} \cdot \delta_{output} \quad (4)$$

The $[M]_{sw}$ and δM_{sw} parameters denote the seawater concentration and isotopic composition of a specific metal (U and Mo), respectively, while 'F' represents the flux. Simplifying the input to river sources and the output to euxinic, ferruginous and (dys)oxic sinks for both elements, we can express the mass balance equations as:

$$\frac{d[M]_{sw}}{dt} = F_{river} - \sum F_i \quad (5)$$

$$\frac{d[M]_{sw}}{dt} \cdot \delta M_{sw} = F_{river} \cdot \delta_{river} - \sum F_i \cdot \delta_i$$

(6)

$$\delta_i = \delta_{sw} + \Delta_i \quad (7)$$

where F_i represents each redox sink, and the sediment isotope (δ_i) composition is derived from the seawater isotopic value and the fractionation between sediment and seawater (expressed as Δ) in different redox settings.

Fluxes into sediments can vary in magnitude based on several factors, including the

areal seafloor extent of the specific redox environment, oceanic elemental concentrations, and the concept of "offshore scaling". This scaling factor assumes that euxinic and ferruginous sinks necessitate progressively larger seafloor areas as they expand into regions with lower organic carbon fluxes *(45)*:

$$F_i = F_{i0} \cdot \left(\frac{A_i}{A_{i0}} \right) \cdot \left(\frac{[M]}{[M]_0} \right) \cdot OSS_i \qquad (8)$$

where A_i represents the areal fraction of each redox sink, with the subscript '0' denoting present-day values, and OSS_i indicates the offshore scaling factor for ferruginous and euxinic sinks.

Two sets of average $\delta^{98}Mo$ and $\delta^{238}U$ values, obtained from oxic red bed intervals and the Ireviken OAE interval, were input into the model. The model was then run 100,000 times, from a present-day initialization under random choices of oxic, reducing and euxinic areal fractions, to investigate the evolution of the areal extent of different redox conditions at steady state, under the initial conditions outlined in Table S6.

Cost function is a mathematical tool used to quantify the discrepancy between model predictions and observed data, which is generally defined as:

$$J(\theta_0,\theta_1) = \frac{1}{2m} \sum_{i=1}^{m} (h_\theta(x^i) - y^i)^2 \qquad (9)$$

The $h_\theta(x^i)$ and y^i parameters are model predicted values and observed values over *m* training examples. θ_0 and θ_1 are model parameters, x^i represents the *i*-th data point, and $h_\theta(x_i) = \theta_0 + \theta_1 x_i$ is the hypothesis function. Minimizing $J(\theta_0,\theta_1)$ ensures the model achieves the best fit by optimizing the intercept (θ_0) and slope (θ_1) to reduce the prediction error. To quantitatively evaluate the agreement between modelled and observed isotopic compositions, we employ the cost function here as:

$$J(\theta_0,\theta_1) = \frac{1}{2m}\sum_{i=1}^{m}\left[\left(\delta^{98}Mo_{model,\,i} - \delta^{98}Mo_{obs,\,i}\right)^2 + \left(\delta^{238}U_{model,\,i} - \delta^{238}U_{obs,\,i}\right)^2\right] \quad (10)$$

The cost function J represents the mean squared error between the modelled and observed isotopic compositions. The terms $\delta^{98}Mo_{(model,i)}$ and $\delta^{238}U_{(model,i)}$ denote the modelled Mo and U isotopic compositions for the i-th simulation, respectively. Similarly, $\delta^{98}Mo_{(obs,i)}$ and $\delta^{238}U_{(obs,i)}$ represent the observed isotopic compositions for the corresponding sample. For this study, $\delta^{98}Mo_{(obs,i)}$ and $\delta^{238}U_{(obs,i)}$ were defined as constant values. For the lower part of the Banwy River section, which reflects marine redox conditions during the mid-Telychian oxygenation interval (Fig. 3), these values are set to the averages of the three samples: $\delta^{98}Mo$ = -1.50‰ and $\delta^{238}U$ = -0.36‰. For samples from the Sheinwoodian ESCIE interval in both sections (Fig. 3), the average isotopic compositions are $\delta^{98}Mo$ = 0.35‰ and $\delta^{238}U$ = -0.28‰. The cost function, J, was minimized over 100,000 iterations, exploring combinations of redox-sensitive parameters to simulate the isotopic response under steady-state conditions. This approach enables the model to produce plausible outputs related to the spatial extent of different marine redox conditions during the studied interval.

References and Notes

1. Calner M. Silurian global events—at the tipping point of climate change. In Mass Extinction (ed. Elewa AMT) 21–58 (Springer, Berlin/Heidelberg, 2008). doi:10.1007/978-3-540-75916-4_4

2. Cooper RA, Sadler PM, Munnecke A, Crampton JS. Graptoloid evolutionary rates track Ordovician–Silurian global climate change. Geological Magazine **151**, 349–364 (2013).

doi:10.1017/S0016756813000198

3. Wang Y, Wignall PB, Xiong Y, Loydell DK, Peakall J, Baas JH, Mills BJW, Poulton SW. Marine redox dynamics and biotic response to the mid-Silurian Ireviken Extinction Event in a mid-shelf setting. Journal of the Geological Society **181**, jgs2023-155 (2024). doi:10.1144/jgs2023-155

4. Cramer BD, Brett CE, Melchin MJ, Männik P, Kleffner MA, McLaughlin PI, Loydell DK, Munnecke A, Jeppsson L, Corradini C, Brunton FR, Saltzman MR. Testing the limits of Paleozoic chronostratigraphic correlation via high-resolution (<500 k.y.) integrated conodont, graptolite, and carbon isotope ($\delta^{13}C_{carb}$) biochemostratigraphy across the Llandovery–Wenlock (Silurian) boundary: Is a unified Phanerozoic time scale achievable? Geological Society of America Bulletin **122**, 1700–1716 (2010). doi:10.1130/B26602.1

5. Lehnert O, Männik P, Joachimski MM, Calner M, Frýda J. Palaeoclimate perturbations before the Sheinwoodian glaciation: A trigger for extinctions during the 'Ireviken Event'. Palaeogeography, Palaeoclimatology, Palaeoecology **296**, 320–331 (2010). doi:10.1016/j.palaeo.2010.01.009

6. Cramer BD, Vandenbroucke TRA, Ludvigson GA. High-resolution event stratigraphy (HiRES) and the quantification of stratigraphic uncertainty: Silurian examples of the quest for precision in stratigraphy. Earth-Science Reviews **141**, 136–153 (2015). doi:10.1016/j.earscirev.2014.11.011

7. Biebesheimer EJ, Cramer BD, Calner M, Barnett BA, Oborny SC, Bancroft AM. Asynchronous $\delta^{13}C_{carb}$ and $\delta^{13}C_{org}$ records during the onset of the Mulde (Silurian) positive carbon isotope excursion from the Altajme core, Gotland, Sweden. Chemical Geology **576**, 120256 (2021). doi:10.1016/j.chemgeo.2021.120256

8. Frýda J, Lehnert O, Joachimski MM, Männik P, Kubajko M, Slavík L, Tonarová P, Černý J. The Mid-Ludfordian (late Silurian) glaciation: A link with global changes in ocean chemistry and ecosystem overturns. Earth-Science Reviews **220**, 103652 (2021). doi:10.1016/j.earscirev.2021.103652

9. Jeppsson L. An oceanic model for lithological and faunal changes tested on the Silurian record. Journal of the Geological Society **147**, 663–674 (1990). doi:10.1144/gsjgs.147.4.0663

10. Lenton TM, Dahl TW, Daines SJ, Mills BJW, Ozaki K, Saltzman MR, Porada P. Earliest land plants created modern levels of atmospheric oxygen. Proceedings of the National Academy of Sciences of the United States of America **113**, 9704–9709 (2016). doi:10.1073/pnas.1604787113

11. Krause AJ, Mills BJW, Zhang S, Planavsky NJ, Lenton TM, Poulton SW, Reinhard CT, Wang X, Weiss A, Daines SJ. Stepwise oxygenation of the Paleozoic atmosphere. Nature Communications **9**, 4081 (2018). doi:10.1038/s41467-018-06504-8

12. Young SA, Kleinberg A, Owens JD. Geochemical evidence for expansion of marine

euxinia during an early Silurian (Llandovery–Wenlock boundary) mass extinction. Earth and Planetary Science Letters **513**, 187–196 (2019). doi:10.1016/j.epsl.2019.02.023

13. Hartke ER, Cramer BD, Calner M, Melchin MJ, Barnett BA, Oborny SC, Johnson EA, Young SA. Decoupling $\delta^{13}C_{carb}$ and $\delta^{13}C_{org}$ at the onset of the Ireviken carbon isotope excursion: $\Delta^{13}C$ and organic carbon burial (f_{org}) during a Silurian oceanic anoxic event. Global and Planetary Change **196**, 103373 (2021). doi:10.1016/j.gloplacha.2020.103373

14. Frieling J, Mather TA, Fendley IM, Jenkyns HC, Zhao Z, Dahl TW, Bergquist BA, Cheng K, Nielsen AT, Dickson AJ. No evidence for a volcanic trigger for late Cambrian carbon-cycle perturbations. Geology **52**, 12–16 (2024). doi:10.1130/G51570.1

15. Reershemius T, Planavsky NJ. What controls the duration and intensity of ocean anoxic events in the Paleozoic and the Mesozoic? Earth-Science Reviews **221**, 103787 (2021). doi:10.1016/j.earscirev.2021.103787

16. Trotter JA, Williams IS, Barnes CR, Männik P, Simpson A. New conodont $\delta^{18}O$ records of Silurian climate change: Implications for environmental and biological events. Palaeogeography, Palaeoclimatology, Palaeoecology **443**, 34–48 (2016). doi:10.1016/j.palaeo.2015.11.011

17. Munnecke A, Samtleben C, Bickert T. The Ireviken Event in the lower Silurian of Gotland, Sweden—relation to similar Palaeozoic and Proterozoic events. Palaeogeography, Palaeoclimatology, Palaeoecology **195**, 99–124 (2003).

514 doi:10.1016/S0031-0182(03)00304-3
515
516 18. Cramer BD, Kleffner MA, Brett CE, McLaughlin PI, Jeppsson L, Munnecke A, Samtleben C,
517 Männik P, Melchin MJ, Corradini C, Brunton FR, Saltzman MR. Paleobiogeography,
518 high-resolution stratigraphy, and the future of Paleozoic biostratigraphy: Fine-scale
519 diachroneity of the Wenlock (Silurian) conodont *Kockelella walliseri*. Palaeogeography,
520 Palaeoclimatology, Palaeoecology **294**, 232–241 (2010).
521 doi:10.1016/j.palaeo.2010.01.002
522
523 19. Jeppsson L, Aldridge RJ, Dorning KJ. Wenlock (Silurian) oceanic episodes and events.
524 Journal of the Geological Society **152**, 487–498 (1995). doi:10.1144/gsjgs.152.3.0487
525
526 20. Loydell DK. Early Silurian sea-level changes. Geological Magazine **135**, 447–471 (1998).
527 doi:10.1017/S0016756898008917
528
529 21. Gelsthorpe D. Microplankton changes through the early Silurian Ireviken extinction event
530 on Gotland, Sweden. Review of Palaeobotany and Palynology **130**, 89–103 (2004).
531 doi:10.1016/j.revpalbo.2003.12.003
532
533 22. Loydell DK, Cave R. The Llandovery–Wenlock boundary and related stratigraphy in
534 eastern mid-Wales with special reference to the Banwy River section. Newsletters on
535 Stratigraphy **34**, 39–64 (1996). doi:10.1127/nos/34/1996/39
536
537 23. Rickards RB. Northern England. In A Global Standard for the Silurian System (eds
538 Holland CH, Bassett MG) 116–131 (National Museum of Wales Geological Series 9,

Cardiff, 1989).

24. Torsvik TH, Cocks LRM. Earth History and Palaeogeography. (Cambridge University Press, 2017). doi:10.1017/9781316225523

25. Loydell DK, Frýda J. Carbon isotope stratigraphy of the upper Telychian and lower Sheinwoodian (Llandovery–Wenlock, Silurian) of the Banwy River section, Wales. Geological Magazine **144**, 1015–1019 (2007). doi:10.1017/S0016756807003895

26. Poulton SW, Canfield DE. Ferruginous conditions: A dominant feature of the ocean through Earth's history. Elements **7**, 107–112 (2011). doi:10.2113/gselements.7.2.107

27. Li S, Wignall PB, Poulton SW. Co-application of rhenium, vanadium, uranium and molybdenum as paleo-redox proxies: Insight from modern and ancient environments. Chemical Geology **674**, 122565 (2025). doi:10.1016/j.chemgeo.2024.122565

28. Rickards RB. On some highest Llandovery red beds and graptolite assemblages in Britain and Eire. Geological Magazine **110**, 70–72 (1973). doi:10.1017/S0016756800047324

29. Hounslow MW, Ratcliffe KT, Harris SE, Nawrocki J, Wójcik K, Montgomery P, Woodcock NH. The Telychian (early Silurian) oxygenation event in northern Europe: A geochemical and magnetic perspective. Palaeogeography, Palaeoclimatology, Palaeoecology **567**, 110277 (2021). doi:10.1016/j.palaeo.2021.110277

30. Matheson EJ, Pufahl PK, Voinot A, Murphy JB, Fitzgerald DM. Ironstone as a proxy of

Paleozoic ocean oxygenation. Earth and Planetary Science Letters **594**, 117715 (2022). doi:10.1016/j.epsl.2022.117715

31. Poulton SW. The Iron Speciation Paleoredox Proxy. (Cambridge University Press, 2021). doi:10.1017/9781108847148

32. Melchin MJ, Sadler PM, Cramer BD. The Silurian Period. In Geologic Time Scale 2020 (eds Gradstein FM, Ogg JG, Schmitz MD, Ogg GM) 695–732 (Elsevier, 2020). doi:10.1016/B978-0-12-824360-2.00021-8

33. Rong J, Wang Y, Zhang X. Tracking shallow marine red beds through geological time as exemplified by the lower Telychian (Silurian) in the Upper Yangtze Region, South China. Science China Earth Sciences **55**, 699–713 (2012). doi:10.1007/s11430-011-4280-0

34. Canfield D. E. The geochemistry of river particulates from the continental USA: Major elements. Geochim. Cosmochim. Acta 61, 3349– 3365 (1997). https://doi.org/10.1016/S0016-7037(97)00172-5.

35. Poulton S. W., Raiswell R. The low-temperature geochemical cycle of iron: from continental fluxes to marine sediment deposition. Am. J. Sci. 302, 774– 805 (2002). https://doi.org/10.2475/ajs.302.9.774.

36. Kendall B, Komiya T, Lyons TW, Bates SM, Gordon GW, Romaniello SJ, Jiang G, Creaser RA, Xiao S, McFadden K, Ristroph M, Reinhard CT, Thompson CJ, Junium CK, Siebert C, Fralick P, Wing BA, Anbar AD. Uranium and molybdenum isotope evidence for an

episode of widespread ocean oxygenation during the late Ediacaran Period. Geochimica et Cosmochimica Acta **156**, 173–193 (2015). doi:10.1016/j.gca.2015.02.025

37. Stockey RG, Cole DB, Planavsky NJ, Loydell DK, Frýda J, Sperling EA. Persistent global marine euxinia in the early Silurian. Nature Communications **11**, 1804 (2020). doi:10.1038/s41467-020-15673-9

38. Dickson AJ, Bagard ML, Katchinoff JAR, Davies M, Poulton SW, Herrle JO. New isotopic constraints on ocean redox at the end of the Eocene. Earth and Planetary Science Letters **562**, 116814 (2021). doi:10.1016/j.epsl.2021.116814

39. Kunert A, Poulton SW, Canfield DE, Fralick PW, Gilleaudeau GJ, Kendall B. Controls on uranium isotope fractionation in the late Paleoproterozoic ocean. Earth and Planetary Science Letters **666**, 119498 (2025). doi:10.1016/j.epsl.2025.119498

40. Anderson R, LeHuray A, Fleisher M, Murray J. Uranium deposition in Saanich Inlet sediments, Vancouver Island. Geochimica et Cosmochimica Acta **53**, 2205–2213 (1989). doi:10.1016/0016-7037(89)90347-3

41. Goldberg T, Archer C, Vance D, Poulton SW. Mo isotope fractionation during adsorption to Fe (oxyhydr)oxides. Geochimica et Cosmochimica Acta **73**, 6502–6516 (2009). doi:10.1016/j.gca.2009.08.004

42. Goldberg T, Archer C, Vance D, Thamdrup B, McAnena A, Poulton SW. Controls on Mo isotope fractionations in a Mn-rich anoxic marine sediment, Gullmar Fjord, Sweden.

Chemical Geology **296**, 73–82 (2012). doi:10.1016/j.chemgeo.2011.12.013

43. Luo J, Long X, Bowyer FT, Mills BJW, Li J, Xiong Y, Zhu X, Zhang K, Poulton SW. Pulsed oxygenation events drove progressive oxygenation of the early Mesoproterozoic ocean. Earth and Planetary Science Letters **559**, 116754 (2021). doi:10.1016/j.epsl.2021.116754

44. Neubert N, Nägler TF, Böttcher ME. Sulfidity controls molybdenum isotope fractionation into euxinic sediments: Evidence from the modern Black Sea. Geology **36**, 775–778 (2008). doi:10.1130/G24959A.1

45. Nägler T, Neubert N, Böttcher M, Dellwig O, Schnetger B. Molybdenum isotope fractionation in pelagic euxinia: Evidence from the modern Black and Baltic Seas. Chemical Geology **289**, 1–11 (2011). doi:10.1016/j.chemgeo.2011.07.001

46. Reinhard CT, Planavsky NJ, Robbins LJ, Partin CA, Gill BC, Lalonde SV, Bekker A, Konhauser KO, Lyons TW. Proterozoic ocean redox and biogeochemical stasis. Proceedings of the National Academy of Sciences of the United States of America **110**, 5357–5362 (2013). doi:10.1073/pnas.1208622110

47. Song Y, Mills BJW, Bowyer FT, Andersen MB, Ossa Ossa F, Dickson AJ, Harvey J, Zhang S, Wang X, Wang H, Canfield DE, Shields GA, Poulton SW. Tracking the spatial extent of redox variability in the mid-Proterozoic ocean. 53, **9**, Geology (2025). doi:10.1130/G53447.1

48. Rutledge RL, Gilleaudeau GJ, Remírez MN, Kaufman AJ, Lyons TW, Bates S, Algeo TJ. Productivity and organic carbon loading control uranium isotope behavior in ancient reducing settings: Implications for the paleoredox proxy. Geochimica et Cosmochimica Acta **368**, 197–213 (2024). doi:10.1016/j.gca.2024.01.007

49. Andersen MB, Stirling CH, Weyer S. Uranium isotope fractionation. Reviews in Mineralogy and Geochemistry **82**, 799–850 (2017). doi:10.2138/rmg.2017.82.19

50. Remírez MN, Gilleaudeau GJ, Gan X, Kipp MA, Tissot FLH, Kaufman AJ, Parente M. Carbonate uranium isotopes record global expansion of marine anoxia during the Toarcian Oceanic Anoxic Event. Proceedings of the National Academy of Sciences of the United States of America **121**, e2406032121 (2024). doi:10.1073/pnas.2406032121

51. Costello MJ, Cheung A, De Hauwere N. Surface area and the seabed area, volume, depth, slope, and topographic variation for the world's seas, oceans, and countries. Environmental Science & Technology **44**, 8821–8828 (2010). doi:10.1021/es1012752

52. Haxen ER, Schovsbo NH, Nielsen AT, Richoz S, Loydell DK, Posth NR, Canfield DE, Hammarlund EU. “Hypoxic” Silurian oceans suggest early animals thrived in a low-O_2 world. Earth and Planetary Science Letters **622**, 118416 (2023). doi:10.1016/j.epsl.2023.118416

53. Cramer BD, Jarvis I. Carbon isotope stratigraphy. In Geologic Time Scale 2020 (Elsevier, 2020) 309–343. doi:10.1016/B978-0-12-824360-2.00011-5

54. Ray DC, Jarochowska E, Hughes HE, Richardson AS, Thomas AT. Glacio-eustatic sea-level changes and their magnitude in the Telychian–Sheinwoodian (Silurian) of England and Wales. Journal of the Geological Society **182**, jgs2024-292 (2025). doi:10.1144/jgs2024-292

55. Jenkyns HC. Geochemistry of oceanic anoxic events. Geochemistry, Geophysics, Geosystems 11, Q03004 (2010). doi:10.1029/2009GC002788

56. Qiu Z, Zou C, Mills BJW, Xiong Y, Tao H, Lu W, Liu X, Xiao S, Poulton SW. A nutrient control on expanded anoxia and global cooling during the Late Ordovician mass extinction. Communications Earth & Environment **3**, 34 (2022). doi:10.1038/s43247-022-00412-x

57. Guilbaud R, Poulton SW, Thompson J, Husband KF, Zhu M, Zhou Y, Shields GA, Lenton TM. Phosphorus-limited conditions in the early Neoproterozoic ocean maintained low levels of atmospheric oxygen. Nature Geoscience **13**, 296–301 (2020). doi:10.1038/s41561-020-0548-7

58. Fan JX, Shen SZ, Erwin DH, Sadler PM, MacLeod N, Cheng QM, Hou XD, Yang J, Wang XD, Wang Y, Zhang YD, Chen Q, Benton MJ, Zhang H, Zhang LN, Shi YK, Yuan DY, Chen XY, Zhou CM, Wen W, Zhang Y, Ke Y, Li GX, Zeng Y, Huang YG, Zhang XL, Wang W, Wang YB, Wang SC. A high-resolution summary of Cambrian to Early Triassic marine invertebrate biodiversity. Science **367**, 272–277 (2020). doi:10.1126/science.aax4953

59. Hallam A, Wignall P. Mass extinctions and sea-level changes. Earth-Science Reviews **48**,

217–250 (1999). doi:10.1016/S0012-8252(99)00055-0

60. Poulton SW, Canfield DE. Development of a sequential extraction procedure for iron: Implications for iron partitioning in continentally derived particulates. Chemical Geology **214**, 209–221 (2005). doi:10.1016/j.chemgeo.2004.09.003

61. Canfield DE, Raiswell R, Westrich JT, Reaves CM, Berner RA. The use of chromium reduction in the analysis of reduced inorganic sulfur in sediments and shales. Chemical Geology **54**, 149–155 (1986). doi:10.1016/0009-2541(86)90078-1

62. Alcott LJ, Krause AJ, Hammarlund EU, Bjerrum CJ, Scholz F, Xiong Y, Hobson AJ, Neve L, Mills BJW, März C, Schnetger B, Bekker A, Poulton SW. Development of iron speciation reference materials for palaeoredox analysis. Geostandards and Geoanalytical Research **44**, 581–591 (2020). doi:10.1111/ggr.12342

63. Pearce CR, Cohen AS, Parkinson IJ. Quantitative separation of molybdenum and rhenium from geological materials for isotopic determination by MC-ICP-MS. Geostandards and Geoanalytical Research **33**, 219–229 (2009). doi:10.1111/j.1751-908X.2009.00012.x

64. Dickson AJ, Jenkyns HC, Porcelli D, van den Boorn S, Idiz E. Basin-scale controls on the molybdenum-isotope composition of seawater during Oceanic Anoxic Event 2 (Late Cretaceous). Geochimica et Cosmochimica Acta **178**, 291–306 (2016). doi:10.1016/j.gca.2015.12.036

65. Stirling CH, Andersen MB, Potter EK, Halliday AN. Low-temperature isotopic fractionation of uranium. Earth and Planetary Science Letters **264**, 208–225 (2007). doi:10.1016/j.epsl.2007.09.019

66. Goldberg T, Gordon G, Izon G, Archer C, Pearce CR, McManus J, Anbar AD, Rehkämper M. Resolution of inter-laboratory discrepancies in Mo isotope data: An intercalibration. Journal of Analytical Atomic Spectrometry **28**, 724–735 (2013). doi:10.1039/C3JA30375F

67. Sun M, Archer C, Vance D. New methods for the chemical isolation and stable isotope measurement of multiple transition metals, with application to the Earth sciences. Geostandards and Geoanalytical Research **45**, 643–658 (2021). doi:10.1111/ggr.12402

68. Tissot FLH, Dauphas N. Uranium isotopic compositions of the crust and ocean: Age corrections, U budget and global extent of modern anoxia. Geochimica et Cosmochimica Acta **167**, 113–143 (2015). doi:10.1016/j.gca.2015.06.034

Acknowledgments: We thank staff at the University of Leeds (Stephen Reid, Andrew Hobson, Robert Jamieson, Fiona Keay, Richard Walshaw, John Wyn Williams, Gary Keech) and at Royal Holloway, University of London (Hannah Elms) for technical assistance. We also thank Robert Newton, Caroline Peacock, Crispin Little, Will Homoky, Tianchen He, Fred Bowyer, Sen Li, Chiara Krewer, Yafang Song and Chong He for valuable discussions and help. We are especially grateful to Thomas and Bethany Wignall for generously assisting with sample collection.

Funding: University of Leeds Research Training Grant (to Y.W.); Natural Environment Research Council grant NE/T008458/1 (to S.W.P.); Yorkshire Geological Society Fearnsides Award (to Y.W.).

Author contributions: Conceptualization, S.W.P., P.B.W., Y.W.; Investigation, Y.W., S.W.P., P.B.W., J.P.; Methodology and laboratory analyses, Y.W., Y.X., A.J.D.; Software and modeling, Y.W., B.J.W.M.; Supervision, S.W.P., P.B.W., B.J.W.M.; Writing original draft, Y.W.; Writing review and editing, all authors, led by P.B.W. and S.W.P.; Data interpretation, all authors.

Competing interests: The authors declare no competing interests.

Data and materials availability: All data generated and analyzed in this study are provided in the Supplementary Materials (Tables S1 to S6). The MATLAB scripts developed for this study were provided to editors and reviewers as supplementary files and will be available from the corresponding author upon reasonable request after publication.